Gas-Phase Flow and Diffusion Analysis of the Droplet-Train/Flow-Reactor Technique for the Mass-Accommodation Processes

Akihiro Morita*

Department of Chemistry, Graduate School of Science, Kyoto University, Kitashirakawa, Sakyo-ku, Kyoto 606-8502, Japan

Masakazu Sugiyama

Department of Electronics Engineering, School of Engineering, University of Tokyo, 7-3-1 Hongo, Bunkyo-ku, Tokyo 113-8656, Japan

Seiichiro Koda

Department of Chemical System Engineering, School of Engineering, University of Tokyo, 7-3-1 Hongo, Bunkyo-ku, Tokyo 113-8656, Japan

Received: July 9, 2002; In Final Form: December 13, 2002

While the droplet-train/flow-reactor method is one of the most powerful experimental techniques to study mass-accommodation kinetics at liquid−vapor interfaces, relatively little is understood about the gas-phase diffusion resistance in the flow tube, an important ingredient to the overall uptake kinetics. In this paper, we theoretically examined the gaseous resistance by numerically solving the coupled-diffusion equation and fluid dynamics in the flow tube. The results indicate that the gaseous resistance for the train of droplets significantly deviates from that for a single spherical droplet because of the interference among the droplets and the flow effect. The dependences of the gaseous transport on varying droplet velocity and orifice frequency are examined and quantitatively elucidated on the basis of the calculated data. This paper suggests that an accurate formula for the gas-phase diffusion resistance is desirable, particularly for the quantitative evaluation of the mass-accommodation coefficients of liquids having substantial vapor pressures.

1. Introduction

The interfacial mass transfer between gaseous and condensed phases is of fundamental importance in heterogeneous atmospheric chemistry and cloud microphysics.[1−4] It has been widely recognized that aerosol particles often play significant roles in the budget and fate of trace gases such as halogens, sulfurs, and organics in the atmosphere via the mass-transfer and surface−bulk reactions, and hence the microscopic understanding of interfacial mass exchange is strongly called for in atmospheric chemistry. The interfacial mass transfer is also of critical significance on the growth rate and composition of the aerosol particles.

Heterogeneous kinetics has been experimentally studied by various techniques,[3,5] for example, the Knudsen-cell reactor,[6−9] droplet-train/flow-reactor,[10−17] coated-wall flow-tube,[18−23] aerosol flow-tube,[24−27] liquid-jet coaxial flow-reactor,[28] and impinging-flow methods.[29] These experiments commonly measure the change in the trace-species concentration due to the interfacial mass transfer. The deposition rate of the trace species is defined as the number of molecules to be taken up per unit time and surface area. The experimental results are expressed by the uptake coefficient γ, defined as the deposition rate normalized by the ideal thermal collision rate ($n_g\bar{c}/4$),

$$\gamma = \frac{\text{deposition rate into the liquid}}{\text{thermal collision rate } (n_g\bar{c}/4)} \quad (1)$$

where, in the denominator, n_g and $\bar{c}$ are the concentration of the trace species in the gas phase and the average thermal velocity of the trace-gas molecules ($=\sqrt{8k_BT/\pi M}$), respectively.

From a microscopic viewpoint, the phenomenological uptake coefficient γ involves following elemental kinetic processes: gas-phase diffusion, mass accommodation, diffusion, and reaction in or on aerosols.[5,30] Therefore, the decomposition of the overall kinetics into the above elemental steps is a critical issue to gain a complete picture of the heterogeneous kinetics. Among the above elemental kinetic steps, the mass-accommodation process of the trace gas after impinging on the surface is truly of an interfacial nature, governed by the molecular properties of the trace gas and surface. This process is characterized by the probability of mass accommodation, namely, the mass-accommodation coefficient

$$\alpha = \frac{\text{amount of trace gas absorbed into the liquid}}{\text{amount of trace gas impinging on the surface}} \quad (2)$$

which ranges from 0 to 1. Thus, deriving α from γ is a crucial concern in the experimental analysis of heterogeneous kinetics.

Among the experimental methods, the droplet-train/flow-reactor technique has been particularly utilized by the Aerodyne and Boston College groups,[10−15] and so far the most comprehensive data have been provided for the mass-accommodation coefficients of a number of species and liquids. The apparatus uses a highly controlled train of droplets passing through a low-pressure flow reactor. The gaseous region of the flow reactor contains the trace species to be taken up, the saturated vapor of

* Corresponding author. Fax: +81-75-753-4000. E-mail: morita@kuchem.kyoto-u.ac.jp.

10.1021/jp021571b CCC: $25.00
Published on Web 02/21/2003

the droplets, and an inert carrier gas such as He or Ar, if necessary. The liquid droplets are generated by a vibrating orifice at a certain frequency and backing pressure. With changes to the orifice frequency, the total surface area of the droplets is well controlled and varied. The uptake amount of the trace gas into the droplets is monitored through the decrease in gaseous concentration, and the uptake coefficient γ is derived from the concentration change with varying total surface area. The droplet-train/flow-reactor technique has important advantages, such as a constantly refreshed liquid surface, precisely controlled surface area, and interaction time in millisecond order. This technique is, therefore, applicable to a wide range of uptake coefficients, including those with relatively large values.

However, the results of the mass-accommodation coefficients appear to be incompatible with other experimental and theoretical results, as is often encountered in heterogeneous chemistry. A microscopic understanding of α is accordingly still far from complete. For example, a serious discrepancy in the ethanol uptake into water has been reported between the experimental value of α[11,12,17] and that calculated via molecular dynamics simulations;[31,32] $\alpha \approx 0.04-0.1$ at room temperature in the former, whereas $\alpha \approx 1$ in the latter. An analogous discrepancy has also been provided among the experimental studies in the ammonia uptake into sulfuric acid solutions.[13,33] As an attempt to elucidate the experimental mass-accommodation coefficients and their temperature dependences, an interesting microscopic model of mass accommodation has been proposed on the basis of the theory of nucleation,[34,35] but this model has not been corroborated by a molecular dynamics simulation.[31] Another remarkable example of our incomplete understanding is the mass-accommodation coefficient α of water into water, which ranges from 0.006 to 1 among the experimental results reported to date.[36,37] The α of water has been drawing considerable attention in the field of cloud microphysics because it is quite relevant to the growth rate of aqueous aerosols,[38,39] but it is still an open and important question whether the α of water into water is considered to be unity or not.[14,36-38] Recently, Li et al.[14] employed droplet-train/flow-reactor experiments using isotopically labeled water ($H_2{}^{17}O$ and D_2O) and argued that the mass-accommodation coefficient could be different from the thermal-accommodation coefficient, probaby for the impinging gas molecule to thermally equilibrate at the surface. They suggested that the former can be smaller than 1, whereas the latter is unity. Evidently, the time scales of the mass and thermal accommodation and the mechanism of proton exchange in the case of water accommodation should be further studied.

The main purpose of the present work is to clarify possible ambiguities in the gas-phase diffusion of the droplet-train/flow-reactor experiments because the gaseous resistance in the experimental analysis involves some important assumptions that might affect the experimentally derived mass-accommodation coefficients. The experimental analysis for the derivation of the mass-accommodation coefficients has been based on the resistance model in the following equation. In this model, the overall resistance of the uptake is decoupled into the resistances of successive processes, that is, the gas-phase diffusion, mass accommodation, and liquid-phase diffusion and reaction[5,30]

$$1/\gamma = 1/\Gamma_g + 1/\alpha + 1/(\Gamma_{sol} + \Gamma_{rxn}) \quad (3)$$

The notations of eq (3) follow those in ref 5, where $1/\gamma$ is the overall resistance and inverse of the uptake coefficient and $1/\Gamma_g$, $1/\alpha$, $1/\Gamma_{sol}$, and $1/\Gamma_{rxn}$ denote the resistances of the gas-phase diffusion, mass accommodation, and liquid-phase solubility and reaction, respectively. Note that eq (3) does not include the surface-specific reaction, which would modify the coupling scheme and the equation.[40] The successive decoupling in eq (3) is shown to be fairly accurate and reliable,[41] essentially because the different resistances in series are attributed to spatially different regions, whereas the parallel connection of Γ_{sol} and Γ_{rxn} in the liquid phase gives some deviation from the exact solution.[5,42] These problems in the surface reaction and liquid phase do not affect the discussion below that focuses on the gas-phase diffusion resistance. We assume the resistance model of eq (3) throughout the following discussion.

The gas-phase resistance $1/\Gamma_g$ for a droplet of diameter d is usually represented by the Fuchs−Sutugin formula[1,43,44] or other alternative formulas.[1] Fuchs and Sutugin gave an analytical formula for gas-phase transport into a spherical particle over a wide range of Knudsen numbers, $Kn = 2l/d$, the ratio of the mean free path of the trace-gas molecules l to the particle radius $d/2$. Assuming $\alpha = 1$, the Fuchs−Sutugin uptake coefficient Γ_{F-S}, normalized by the surface area $4\pi(d/2)^2$ and the thermal collision rate $n_g\bar{c}/4$, is given as

$$\Gamma_{F-S} = \frac{4\pi(d/2)D_g n_g}{1+\lambda Kn}\Big/\left[4\pi(d/2)^2\frac{n_g\bar{c}}{4}\right] = \frac{4Kn}{3}\frac{1}{1+\lambda Kn} \quad (4)$$

where D_g is the gas-phase diffusion coefficient of the trace gas and λ denotes correction from the purely diffusive transport,

$$\lambda = (1.333 + 0.71Kn^{-1})/(1 + Kn^{-1}) \quad (5)$$

In eq (4), Meyer's expression for the diffusion coefficient, $D_g = l\bar{c}/3$, is employed so that $Kn = 6D_g/\bar{c}d$. The gas-phase resistance $1/\Gamma_g$ is thus represented as

$$\frac{1}{\Gamma_g} = \frac{1}{\Gamma_{F-S}} - 1 = \frac{0.75 + 0.283Kn}{Kn(1+Kn)} \rightarrow \frac{0.75}{Kn} - 0.467 \quad (Kn \rightarrow 0) \quad (6)$$

The limiting formula of the right-hand side of eq (6) corresponds to the continuum expression[5]

$$1/\Gamma_g = \bar{c}d/8D_g - {}^1/_2 \quad (7)$$

The first term of eq (7) is derived by solving the steady-state diffusion equation in the spherical boundary condition, and the second term stems from the kinetic correction.[5,45] The difference between eqs (6) and (7) is not significant in the case of the water droplets discussed below, due to the saturated water vapor pressure reducing the mean free path and the Knudsen number ($Kn \lesssim 0.2$ at $T = 0$ °C). The present paper deals with the continuum regime most often encountered in atmospheric chemistry, while the intermediate or kinetic regime with higher Kn values has recently been explored using sulfuric acid or organic liquids in laboratory experiments.[15]

However, eq (6) or (7) involves the important assumption that the concentration distribution is spherical around a single static droplet, whereas in the droplet-train flow tube the fast-moving train of droplets would break the spherical symmetry. Therefore, it has not been obvious whether eq (6) can be properly applied to the droplet-train/flow-reactor conditions. Such effects were discussed by Widmann and Davis,[46] but they modeled the droplet train as a liquid rod, which should be the other extreme situation, exaggerating the interference of the droplets. In the actual experimental conditions, the gas-phase diffusion resistance is minimized using low pressure (high D_g) and small droplets (small d), but the gas-phase resistance is still substantial for the water droplets near room temperature. The

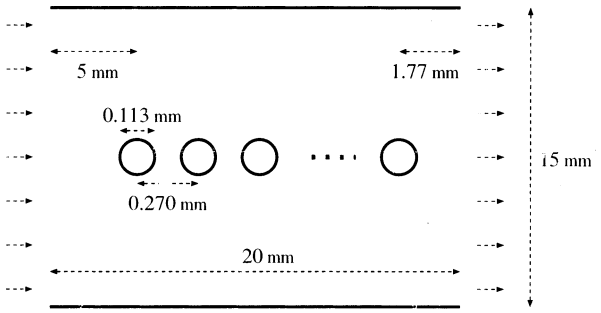

Figure 1. Cross section of the cylindrical flow tube with the standard geometry with units of millimeters. The wall and the gaseous flow move to the right relative to the droplets.

purpose of the present paper is to quantitatively evaluate the gas-phase resistance in the droplet-train/flow-reactor apparatus. We numerically solved the coupled-diffusion equation and the fluid dynamics for flow conditions that mimic the droplet-train/flow-reactor apparatus. As we will see, the deviation of the trace-gas-phase concentration from a spherical distribution is, in fact, observed, which influences the gas-phase resistance for the trace-gas uptake. We recently published a first report of the numerical analysis in a short letter,[47] and the present paper provides a more comprehensive presentation of the calculations and expands the discussion and analysis by systematically changing the geometry and conditions.

The remainder of this paper is as follows. The next section describes the method and conditions of the calculations, and section 3 presents the results and discussion. Brief concluding remarks follow in section 4.

2. Method

The calculations were performed in the boundary conditions that correspond to a typical droplet-train/flow-reactor apparatus. The train of water droplets is assumed to be generated from an orifice of diameter $d_o = 60$ μm at velocity $v_d = 27$ m/s and frequency $f_o = 100$ kHz.[10] These parameters, satisfying the Rayleigh formula of natural breakup[10]

$$f_o = v_d/4.5d_o \tag{8}$$

are specified as a standard configuration of the droplet train in this work, though the effects of the varying parameters on the uptake kinetics will also be discussed later. The distance between adjacent droplet centers d_c is, consequently, $d_c = v_d/f_o = 270$ μm. The volumetric flow rate of the liquid water F is represented twofold,

$$F = \pi(d_o/2)^2 v_d = {}^4/_3\pi(d/2)^3 f_o \tag{9}$$

which derives the droplet diameter d in the natural breakup condition as

$$d = (3d_o{}^2 v_d/2f_o)^{1/3} = (3 \times 4.5/2)^{1/3} d_o \approx 1.89d_o \tag{10}$$

Equation (10), in connection with the orifice diameter $d_o = 60$ μm, leads to the droplet diameter $d = 113$ μm. The standard geometry of the flow tube is depicted in Figure 1, where 50 droplets are aligned on the center of a spherical cylinder with a diameter of 15 mm and a length of 20 mm. The train of droplets moves left at a relative speed v_d to the cylinder wall. The gaseous volumetric flow rate was set at 200 cm^3/s in the same direction, which means the gas velocity is $v_g = 200$ cm^3/s/[π(15 mm/2)^2] = 1.13 m/s. For practical convenience of calculations, the droplets were fixed while the wall and the gaseous flow moved to the right by v_d and $v_d - v_g$, respectively (see Figure 2a).

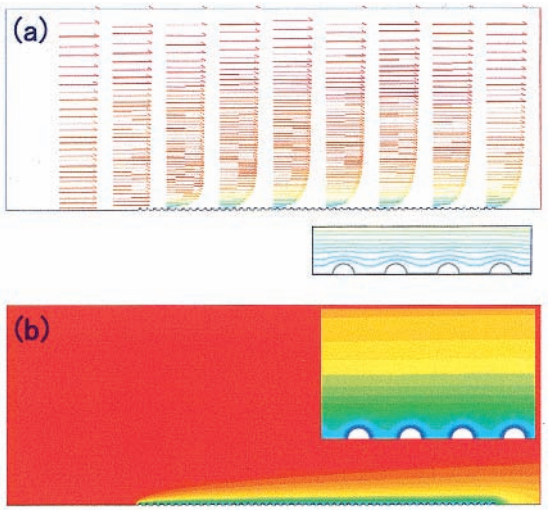

Figure 2. (a) Velocity field of the gas flow relative to the droplets and (b) trace-gas concentration in the flow tube with the standard geometry depicted in Figure 1 at steady state with the temperature $T = 0$ °C, the total pressure $P_{total} = 25$ Torr, and He buffer. Half the cross section along the tube axis is displayed, where the top line denotes the cylindrical wall surface and the bottom line the central axis of the flow tube. The magnified picture in panel a shows the streamlines in the vicinity of the 46−49th droplets (from the left). The inset in the upper right corner of panel b shows the concentration in the vicinity of the 46−49th droplets.

We note that the diameter of the flow tube in Figure 1 corresponds to the actual experiments, while the length is substantially shorter because of computational limitations. To eliminate possible artificial influences of the finite tube length on the velocity field, the stationary velocity field in a long flow tube without the droplets was calculated prior to the droplet calculations in a cylindrical tube with the same diameter (15 mm) and sufficient length (320 mm). The stationary velocity field thus developed near the outlet side of the long tube, which has a parabolic velocity distribution with v_d at the wall surface and with the average of $v_d - v_g$, was utilized as the boundary condition of the droplet-train flow tube at the gas-inlet side (left side in Figure 1). The boundary condition at the outlet side (right side in Figure 1) was a constant pressure identical to that of the bulk. We applied a nonslip boundary condition to the gaseous flow on the surface boundary of the wall and the droplets throughout. The temperature was assumed to be uniform in the flow tube because the trace amount of the uptake gas should produce a negligible heat of condensation.

The gas in the flow tube consists of the trace species for uptake, water vapor, and inert carrier gas, if necessary. The trace gas was modeled as methanol at an initial concentration $n_g = 10^{13}$ molecules/cm^3 at the inlet. The trace-gas concentration is low enough to safely neglect its influence on the flow field, and we confirmed the linearity of the uptake in trace-gas concentration by examining another concentration, 5×10^{13} molecules/cm^3. The gas in the flow tube should be saturated with water vapor, and three cases of the vapor pressure were examined depending on the temperature: 12.8, 4.6, and 1.7 Torr at $T = +15$, 0, and -13 °C, respectively.[5,48] The carrier gas was either He or Ar to maintain the total pressure inside the flow tube in the range of 6−50 Torr. The Reynolds numbers of the above situations are below 10.0, which allows us to treat the situation as having laminar flow.

The intrinsic deposition rate constant of the trace species onto the droplet surface, k^{int}, is defined as the deposition rate

normalized with the local gas-phase concentration at the droplet surface. We modeled the rate constant in two ways, perfect uptake and a finite rate $k^{int} = \bar{c}/2$. The former assumption indicates that the uptake resistance is determined solely by the gas-phase resistance, $1/\gamma = 1/\Gamma_g$. In the calculations, this assumption of perfect uptake was implemented with sufficiently large values as $k^{int} = 10^{30}-10^{35}$cm/s, which imposes vanishing concentration of the trace species at the droplet surface, consistent with the absorbing boundary condition of the conventional Smoluchowski theory.[49] We confirmed that the concentration field and the deposition rate are invariant with k^{int} in the above range. The latter assumption of $k^{int} = \bar{c}/2$, on the other hand, effectively incorporates the finite kinetic collision rate at the interface in the Collins−Kimball boundary condition.[50] The intrinsic rate constant $\bar{c}/2$, twice as large as the ideal thermal collision-rate constant $\bar{c}/4$, is consistent with the unit mass-accommodation coefficient $\alpha = 1$, considering that the surface uptake distorts the isotropic Maxwell−Boltzmann molecular velocity distribution near the interface.[51] (Note that the same mechanism also accounts for the term $^1/_2$ in eq (7).)[45] Although the two assumptions make little difference in the flow or concentration field, special care has to be taken of the interfacial resistance when examining the possible uncertainty in the mass-accommodation coefficient derived in the flow conditions. For this purpose, the latter assumption of the finite k^{int} should be employed.

Besides the standard geometry depicted in Figure 1, we also examined other geometries for comparison to determine the effects of varying parameters, particularly the droplet velocity and the orifice frequency. To cover the experimental range of the droplet velocity, two droplet velocities of 15 and 44 m/s were employed in addition to the standard velocity, $v_d = 27$ m/s. Regarding the orifice frequency, two other frequencies, $f_o/4$ and $f_o/16$, were also employed in addition to the natural breakup frequency f_o, with a fixed liquid volumetric flow rate and droplet velocity. Although the Rayleigh natural breakup condition of eq (8) is no longer satisfied for other frequencies, these subharmonic frequencies of the natural breakup are efficient enough to generate the droplets and are actually utilized in the experiments.[10,15] For these alternative frequencies, the droplet diameter d and the distance d_c simultaneously change as $d \propto f_o^{-1/3}$ and $d_c \propto f_o^{-1}$, which in turn change the total droplet surface area $\propto f_o^{1/3}$. In the calculations with the lower frequencies, the tube length was enlarged to 400 and 900 mm for $f_o/4$ and $f_o/16$, respectively, as the droplet distance d_c increases, so that the former tube segment contains 40 droplets and the latter segment contains 20 droplets.

The viscosity of the fluid and the diffusion coefficients of the constituent molecules at each pressure and temperature were evaluated via the Chapman−Enskog theory.[52,53] The collision integrals were calculated with the Stockmeyer model for the polar molecules and the Lennard-Jones model for the nonpolar molecules, where the ingredient parameters were taken from the literature.[54] The calculated diffusion coefficients for varying composition, pressure, and temperature are given in Table 1.

The coupled-fluid and -diffusion equations were numerically solved using the FLUENT package[55] in the axisymmetric two-dimensional space. In the finite-volume approach, special care was taken to describe the boundary region near the gas−droplet interface, the critical gas-phase region for the uptake. The boundary region was divided radially with six concentric circles, which were then divided evenly at a constant angle of 180°/10 = 18° to define the volume elements. The closest circle corresponds to the droplet surface, and the radial spacings between adjacent circles were 11.0, 12.1, 13.3, 14.6, and 16.1 μm, which gradually increase as the circles become farther away from the droplet. The rest of the gas-phase space was divided into triangular volume elements, and the total number of the volume elements was 64 413 for the flow tube in Figure 1. To check the accuracy of the above finite mesh division, we used another finer mesh division, consisting of 110 626 quadrilateral elements, for comparison and confirmed that the calculated deposition rates for the two schemes of mesh divisions agreed within 0.5%. For the discretization method, the first-order upwind scheme[55] was employed, where the concentration and its gradient at the droplet surface are represented with the cell-center values at the volume elements in contact with the surface. More exactly, however, the deposition rate should be derived from the values at the droplet surface, which correspond to the edges of the cells in the discretization method. Therefore, we examined the accuracy of the calculated deposition rate by comparing this method with the second-order upwind scheme, which extrapolates the cell-center values to those at the edges of the cell, and found that the two results agreed within 4%.

TABLE 1: Calculated Diffusion Coefficients, D_g, for the Trace Gas Methanol with Varying Temperature and Gas Composition[a]

T (°C)	P_{total} (Torr)	P_{buffer} (Torr)	D_g (m^2/s)
(a) −13	6.0	4.3 (He)	2.88×10^{-3}
	25.0	23.3 (He)	1.13×10^{-3}
	50.0	48.3 (He)	6.31×10^{-4}
	25.0	23.3 (Ar)	3.48×10^{-4}
(b) 0	6.0	1.4 (He)	1.68×10^{-3}
	25.0	20.4 (He)	9.21×10^{-4}
	50.0	45.4 (He)	5.78×10^{-4}
	25.0	20.4 (Ar)	3.75×10^{-4}
(c) +15	12.8	0.0 (−)	7.18×10^{-4}
	25.0	12.2 (He)	5.95×10^{-4}
	50.0	37.2 (He)	4.41×10^{-4}
	25.0	12.2 (Ar)	3.94×10^{-4}

[a] Note that the saturated water vapor pressures are (a) 1.7, (b) 4.6, and (c) 12.8 Torr. The concentration of the trace gas methanol is fixed at 10^{13} molecules/cm^3.

3. Results and Discussion

3.1. Gaseous Velocity and Concentration Fields. Figure 2a displays the velocity field of the gas flow in the flow tube at a steady-state condition. Because this figure adopts a relative velocity to the fixed droplets as mentioned in section 2, the gas velocity at the wall surface (top line of the panel) is fixed at $v_d = 27$ m/s, and the average gas velocity at the inlet side (left side) is $v_d - v_g = 25.87$ m/s along the axis. Panel a shows a nearly uniform gaseous velocity distribution, parallel to the axis, except for in the vicinity of the train of droplets (bottom line), where significant perturbation on the gaseous flow by the droplets is apparently observed. Note that the gaseous velocity between adjacent droplets on the axis almost vanishes at steady state, which implies that the gas flow exerts little local shear friction on the droplet movement. This is consistent with the experimental evidence that the train of droplets suffers from little deceleration at steady state.[15] (More rigorously, a slight change in the droplet speed is actually observed.[12] The possible effects associated with the droplet deceleration are discussed in appendix A.)

The flow field in the perturbed region is further observed in the magnified picture of Figure 2a, which displays the streamlines in the vicinity of the droplets. The streamlines are generally parallel to the axis even in the perturbed region, while the corrugated lines are seen in the vicinity of the droplet train.

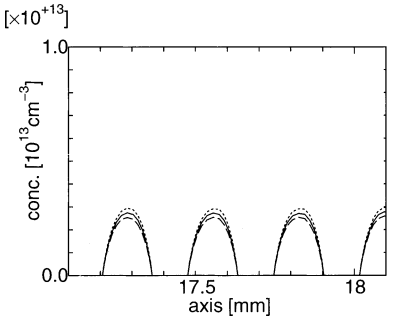

Figure 3. Trace-gas concentration on the axis of the flow tube at 0 °C. The dashed line, solid line, and dotted line refer to the total pressures P_{total} of 6, 25, and 50 Torr, respectively. The origin of the abscissa corresponds to the left end of the flow tube in Figure 1. Note that the regions having no finite concentration correspond to the droplets.

The parallel streamlines imply that the mass transport along the radial direction is mostly attributed to diffusion. The slight corrugation is induced by the droplet-train motion. After a droplet sweeps out a volume of gas, the droplet's trailing wake partially draws in gas, but the gas stream does not fully replenish the trace gas near the center line of the droplet stream before the next droplet arrives. The figure manifests fluid dynamical coupling among the droplets, significantly affecting the velocity field inside the flow tube. One can expect that it should also affect the trace-gas concentration field and the mechanism of gaseous transport.

The spatial distribution of the trace-gas concentration is shown in Figure 2b. The concentration field in the whole flow tube is characterized by a remarkable depletion in the trace species near the axis, with an enhanced gradient along the radial direction. This is because the axial transport is relatively fast because of the velocity field, whereas the radial transport is mostly diffusional. Consequently, the concentration field assumes nearly cylindrical symmetry as a whole. At closer dimensions, however, the magnified picture in Figure 2b shows a roughly spherical concentration field around each droplet within the distance nearly equal to the droplet radius, though the concentration field is somewhat distorted by the droplet translational motion. Figure 3 displays the trace-gas concentration on the flow-tube axis. Because each droplet is surrounded by the depleted region in the trace species and the droplets are fairly closely spaced, the tail distributions of the neighboring droplets overlap each other. Consequently, the maximum concentration in the middle of the droplets is substantially reduced below the bulk value, $n_g = 10^{13}$ molecules/cm^3 (upper bound of Figure 3), due to the interference among the droplets.

Figure 3 also shows the pressure dependence on the concentration profile. Although the concentration profile is not sensitive to the varying total pressure, the maximum concentration in the middle of the droplets slightly increases with the total pressure. It is qualitatively understood from the Rantz−Marshall formula[56] (compare with section 3.4) that the surface boundary layer around each droplet becomes thinner with increasing pressure, thereby reducing the overlap of the tails.

3.2. Deposition Rates. In the preceding subsection, we observed that the velocity and the trace-species concentration distribution of the gas in the flow tube evidence considerable differences from the ideal situation where a single, independent droplet is located in static gaseous media. This subsection discusses how these features in the gaseous concentration fields affect the deposition rate of the trace gas into the droplets. The boundary condition of perfect uptake is adopted at the droplet surface in section 3.2 to focus on the gaseous resistance.

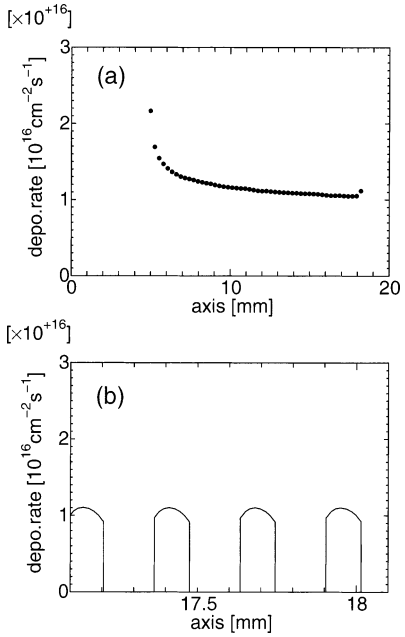

Figure 4. Spatial dependence of the trace-gas deposition rate into the droplets at the same conditions as Figure 2. Each point in panel a denotes the deposition rate into each droplet, and panel b displays the deposition rate as a function of the axial position.

First, we discuss the spatial dependence of the deposition rate in the flow tube. Figure 4a exhibits the deposition rates of the 50 droplets that are not exactly identical with respect to their location in the flow tube. Each data point in Figure 4a represents the averaged deposition rate over a whole droplet sphere, $\bar{R}(z_0)$. The spherical average was taken for each droplet as

$$\bar{R}(z_0) = \frac{1}{d}\int_{z_0-d/2}^{z_0+d/2} R(z)\,\mathrm{d}z \qquad (11)$$

where z_0 is the axial center-of-mass coordinate of the droplet. Note that the axial coordinate z uniquely determines the deposition rate $R(z)$ at the droplet surface because of the cylindrical symmetry. Figure 4a shows a nearly constant rate except for a few upstream droplets and the last downstream one. Exceptional rates could be observed in the droplets of both ends, where lack of the translational symmetry is most pronounced. The deviation is more obvious in the upstream droplets because the cylindrical concentration field has not fully grown upstream as shown in Figure 2b. These exceptional values should be disregarded to discuss the representative rate in the flow tube. The deposition rate is almost constant in the middle, whereas careful observation reveals a slight decrease in the rate along the flow, implying that the convergence is not completely reached within the calculated flow-tube length. We took the representative deposition rate as that from the downstream droplets except for the last few, but this value should be regarded as an upper limit of the true deposition rate (see appendix B).

Close observation of the downstream droplets is provided in Figure 4b, a magnified picture of the deposition rate as a function of the axial position, where nonzero values appear only in the region occupied by the droplets. Although this figure shows a slightly larger rate at the droplet side than that at the head or tail, the difference is not very significant, implying a nearly uniform deposition rate around the droplet surface. We will deal with the spherically averaged deposition rate of the downstream droplets in the following discussion.

The deposition rates with varying total pressure P_{total}, temperature T, and buffer gas are summarized in Figure 5. The

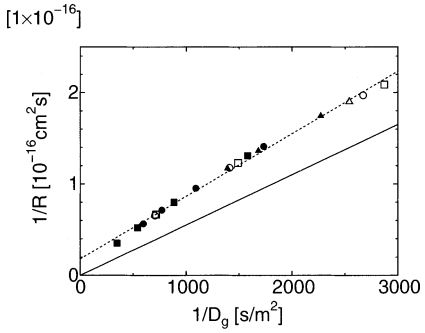

Figure 5. Relation between the inverse diffusion coefficient $1/D_g$ and inverse deposition rate $1/R$ of the model for methanol uptake with varying total pressure P_{total}, temperature T, and buffer gas. The square, circle, and triangle points indicate $T = -13$, 0, and $+15$ °C, respectively; the solid and open symbols denote He and Ar buffer gases. The solid line refers to the ideal deposition rate $1/R_{ideal}$ of eq (12), and the dotted line is a least-squares-fitted linear regression line.

data points due to the varying parameters noted above are well characterized by a single parameter, the gas-phase diffusion coefficient of the trace species D_g. This is reasonable, provided that the fluid dynamical fields influencing the deposition rate change little for the range of parameters studied, which appears to be consistent with our observation that the velocity and concentration fields of the gas are insensitive to the range of the temperatures and pressures examined.

Another remarkable feature in Figure 5 is the systematic upward deviation of the computed data points from the solid line due to

$$1/R_{ideal} = d/2D_g n_g = (\bar{c}d/8D_g)/(n_g\bar{c}/4) \qquad (12)$$

which denotes the ideal deposition rate derived from the Smoluchowski theory. This equation is equivalent to eq (7) except for the kinetic correction term $-1/2$, which is not included in eq (12) on the basis of the perfectly absorbing boundary condition. The systematic upward deviation indicates an augmented resistance of the gas-phase transport. This is attributed to the interference among the droplets, as discussed in section 3.1. Figure 2b demonstrated that the train of droplets tends to develop a cylindrical concentration field, involving larger concentration gradients in the radial direction than in the axial direction. Subsequently, the diffusive transport is effectively restricted to a two-dimensional space except in the axial direction. The restricted transport results in the augmented resistance, compared to the free, three-dimensional diffusion represented by eq (12).

Figure 5 shows a linear regression line determined by the least-squares fitting of the calculated data. The dotted line has an apparent nonzero intersection at the y axis, and its slope is larger than that of the solid line, eq (12). Implications of these features will be discussed in section 3.3. While the optimized linear line roughly reproduces the calculated deposition rates, close observation reveals a slight convex feature of the calculated data toward the origin. This implies that a better expression of the gas-phase resistance should be provided by a nonlinear formula with the convex feature and extrapolation to the origin. We plan to provide an accurate and practical formula for the gas-phase resistance as a function of the droplet geometry and conditions. Possible uncertainties in the calculated deposition rates are discussed in detail in appendix B.

3.3. Uptake and Mass-Accommodation Coefficients. This subsection analyzes uptake and mass-accommodation coefficients measured with the droplet-train flow reactor. The main goal here is to improve the analysis for experimental mass-accommodation coefficients using a more accurate and quantitative description of the gaseous resistance. Because the present discussion aims at evaluating the interfacial resistance, we adopt the finite intrinsic deposition rate $k^{int} = \bar{c}/2$ for the boundary condition at the droplet surface in this subsection. This effectively accounts for the unit intrinsic mass-accommodation coefficient at the droplet surface, $\alpha = 1$, as discussed in section 2. The diffusion equation and fluid dynamics were simulated at $T = 0$ °C with varying pressure, and the calculated deposition rates were normalized by $n_g\bar{c}/4$ to derive the uptake coefficients γ.

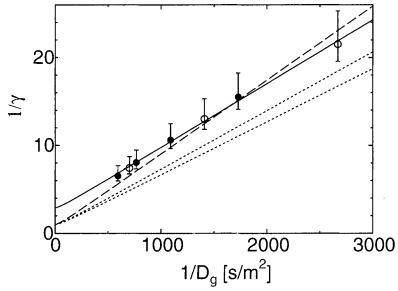

Figure 6. Relation between the inverse diffusion coefficient $1/D_g$ and inverse uptake coefficient $1/\gamma$ of methanol at $T = 0$ °C. The solid and open circles denote respectively He and Ar buffer gases with varying pressure. The solid line is the analytical expression for eq (13) with the optimized $d_{eff} = 137$ μm and $\alpha_{eff} = 0.35$ and the dashed line with the optimized $d_{eff} = 159$ μm and $\alpha_{eff} = 1$ fixed. The two dotted lines show the range defined by $d_{eff} = 114-126$ μm and $\alpha_{eff} = 1$.

The uptake coefficients γ were expressed analytically by the resistance model, eq (3), and the Fuchs−Sutugin formula, the left-hand side of eq (1),

$$\frac{1}{\gamma} = \frac{1}{\Gamma_g} + \frac{1}{\alpha} = \frac{0.75 + 0.283Kn}{Kn(1+Kn)} + \frac{1}{\alpha}, \quad Kn = \frac{6D_g}{\bar{c}d} \qquad (13)$$

This equation does not account for the resistance in the liquid phase, Γ_{sol} or Γ_{rxn} in eq (3), because the present calculations include only the gaseous and interfacial resistances. Though eq (13) employs the full Fuchs−Sutugin formula of eq (1), using the limiting formula (right-hand side) of eq (1) or the continuum representation of eq (7) makes little difference in the following discussion, which justifies the diffusive treatment of the gaseous resistance.

The calculated uptake coefficients γ were fitted by eq (13) via the optimization of two parameters, d (or Kn) and α, and the results are plotted in Figure 6. Note that the two parameters, the effective droplet diameter d_{eff} and the effective mass-accommodation coefficient α_{eff}, approximately correspond to the slope and the intersection of the ordinate, respectively, in Figure 6. The solid line of Figure 6 is the optimized result by the least-squares fitting; $d_{eff} = 137$ μm, and $\alpha_{eff} = 0.35$. The effective droplet diameter optimized to the gaseous resistance, d_{eff}, is considerably larger than the real diameter $d = 113$ μm by 20%. The notion of the effective diameter in the droplet-train flow tube has been proposed by Worsnop et al.,[15] and they assumed the effective diameter to be twice the orifice diameter, that is, $2d_o = 120$ μm in this case, also somewhat larger than the real diameter. The present calculation qualitatively supports this experimental assumption, while the optimized diameter, $d_{eff} = 137$ μm, is a little larger than twice the orifice diameter, $2d_o$.

Next, we discuss the uncertainties inherent in the optimized parameters derived above. The uncertainties in the calculated deposition rates are extensively discussed in appendix B, and the results are shown in Figure 6 by the error bars of the

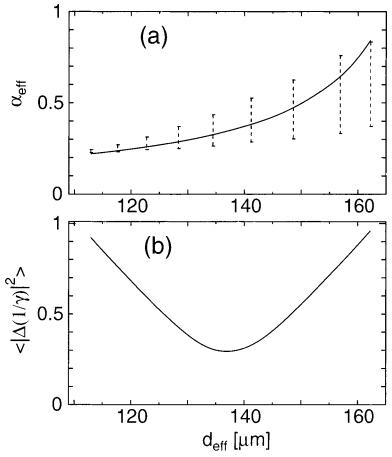

Figure 7. (a) Optimized mass-accommodation coefficient α_{eff} as a function of the effective diameter d_{eff}, derived from Figure 6. The possible range of α_{eff} is shown with the dashed bars. (b) Root-mean-square deviation for the least-squares fitting.

calculated data points of $1/\gamma$. These uncertainties in $1/\gamma$ should affect the uniqueness of the optimized parameters of α_{eff} and d_{eff}. Figure 7 shows the effective mass-accommodation coefficient as a function of d_{eff}, determined by the least-squares fitting at each fixed value of d_{eff}. The root-mean-square deviation $\langle|\Delta(1/\gamma)|^2\rangle$ in the least-squares fitting is also shown in panel b. Considering the uncertainties in $1/\gamma$, as given in Figure 6, the effective mass-accommodation coefficient can be defined in the range of $d_{eff} = 113-163$ μm, and possible values of α_{eff} are shown with the dashed bars in Figure 7a. Figure 7 indicates that the value of the effective diameter originally proposed, $d_{eff} = (2.0 \pm 0.1)d_o = 114-126$ μm, is acceptable within the error range, while the fitting accuracy is not as good as that by the best fit ($d_{eff} = 137$ μm). However, the original value of $d_{eff} = 114-126$ μm should yield $\alpha_{eff} = 0.22-0.34$, and $\alpha_{eff} = 1$ in combination with $d_{eff} = 114-126$ μm does not reproduce the calculated uptake coefficient, as shown by the dotted lines in Figure 6.

The effective mass-accommodation coefficient α_{eff} is a controversial notion because it appears to be inconsistent with $\alpha = 1$, the intrinsic mass-accommodation coefficient assumed for the boundary condition of the calculation discussed in this subsection. Therefore, α_{eff} should be regarded as a provisional mass-accommodation coefficient obtained from the conventional analysis based on the Fuchs−Sutugin formula. To examine further the effective mass-accommodation coefficient, we fit eq (13) with $\alpha_{eff} = 1$ fixed, and the result is displayed in Figure 6 as the dashed line. When the two fitted lines are compared, it is found that the dashed line is not acceptable, because the dashed line does not reproduce all the calculated data points within the error bars. The dashed line corresponds to an effective droplet diameter of 159 μm, substantially larger than the real diameter of 113 μm or the optimized effective diameter of 137 μm. The above discussion manifests the necessity of a more accurate and quantitative evaluation of the gaseous resistance than that of the Fuchs−Sutugin formula for the droplet-train flow reactor.

We expand on the above outcome with three important comments. First, the above discussion is entirely based on a continuum flow description of gaseous transport, whereas the original purpose of the Fuchs−Sutugin formula was to describe gaseous transport over a wide range of Knudsen numbers. The problem illustrated above could be experimentally removed if a sufficiently low flow-reactor pressure were utilized because the gaseous resistance becomes asymptotically negligible with increasing Knudsen number. Such conditions have been explored using sulfuric acid or organic liquids having low vapor pressures.[15] Second, measuring the mass-accommodation coefficients in the continuum regime is increasingly difficult as α becomes larger, close to unity.[57] The uncertainty of the analysis is more pronounced for larger values of α, and the above condition of $\alpha = 1$ is an extreme case, where the uncertainty is most pronounced. However, sometimes one wants to measure a relatively large α when the gaseous resistance is necessarily substantial, for example, because of water vapor on liquid water, and only in such cases will the accurate evaluation of the gaseous resistance have significant consequences. Third, an interesting problem remains in the uptake associated with the H−D isotope exchange.[12,14] The uptake of the deuterated species, CD_3COOD or D_2O, is reported to be faster than that of the normal counterpart. The mechanism of the enhanced uptake is not elucidated by the present analysis, and further work is needed.

3.4. Effects of Droplet Velocity. The last two subsections, sections 3.4 and 3.5, deal with the deposition rate with varying droplet velocity and orifice frequency, respectively. The actual droplet-train/flow-reactor experiments often utilize these varying conditions, which should significantly affect the gaseous fields in the flow tube. Therefore, it is meaningful to theoretically examine their influences on the deposition rate. The discussion in the last two subsections is based on the absorbing boundary condition at the droplet surface to focus on the gas-phase resistance, though a difference in the boundary condition does not affect the following discussion.[58]

Droplet movement amplifies the interference among the droplets, causing the break in spherical symmetry around a droplet. That is, while we have emphasized the interference among the droplets in the flow tube, the interference is actually coupled to the flow field induced mainly by the droplet movement. This subsection examines the flow-field effect in connection with the interference effect by varying the droplets' velocities.

Figure 8 shows the $1/D_g-1/R$ plots with varying droplet velocity v_d in the experimental range of 15−44 m/s.[10] The calculated deposition rates (solid symbols) yield a slight dependence on the droplet velocity in this range. The results are qualitatively consistent with the experimental finding that the v_d dependence on the uptake is not significant,[10] but Figure 8 suggests that the dependence should be taken into account in the quantitative analysis of the gaseous resistance.

The next issue is to provide a quantitative model to elucidate the v_d dependence on the deposition rate. A simple and useful model that incorporates the flow effect is provided by the Rantz−Marshall formula,[56] which represents the deposition rate R_{R-M} using the Sherwood number, *Sh*, as follows:

$$1/R_{R-M} = d/ShD_g n_g \tag{14}$$

$$Sh = 2 + 0.6(\rho v d/\mu)^{1/2}(\mu/\rho D_g)^{1/3} \tag{15}$$

where $v = v_d - v_g$, the droplet velocity relative to the background gaseous flow. ρ and μ denote the mass density and viscosity of the gas, respectively. Note that eqs (14) and (15) coincide with eq (12) at $v = 0$, which indicates that the Rantz−Marshall formula is a natural extension of the Smoluchowski diffusion-theory formulation. The flow effect is expressed in the previous equations through the Sherwood number, *Sh*, deviating from 2. The Sherwood number refers to the inverse thickness of the surface boundary layer relative to the droplet diameter. Equations (14) and (15) indicate that the faster flow velocity v leads to the larger *Sh* and, hence, a larger deposition

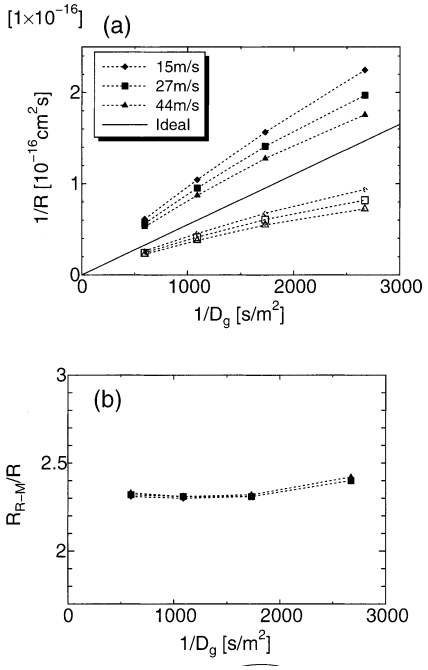

Figure 8. (a) Relation between the inverse diffusion coefficient $1/D_g$ and inverse deposition rate $1/R$ of the model with methanol as the trace gas and varying total pressure P_{total} and droplet velocity v_d at $T = 0$ °C. The diamond, square, and triangle points denote $v_d = 15$, 27, and 44 m/s, respectively. The solid symbols indicate the calculated values and the open ones the Rantz−Marshall values $1/R_{R-M}$ of eqs (14) and (15). The solid line refers to the Smoluchowski deposition rate $1/R_{ideal}$ of eq (12), and the dotted lines connect the symbols to guide the eye. Panel b shows the ratio R_{R-M}/R.

rate R_{R-M}, implying that the thinner boundary layer facilitates gaseous deposition onto the droplet surface.

Figure 8 also displays the inverse Rantz−Marshall deposition rate $1/R_{R-M}$ (open symbols) with varying diffusion coefficient and droplet velocity. The Rantz−Marshall formula provides the inverse deposition rate $1/R_{R-M}$ considerably below the inverse Smoluchowski diffusive rate $1/R_{ideal}$, indicating that the flow effect generally facilitates the deposition. Equations (14) and (15) quantitatively reproduce the velocity dependence of the deposition rate fairly well, with a scaling factor $R_{R-M}/R \approx 2.3-2.4$ nearly invariant over the range of the diffusion coefficients and droplet velocities we considered.

The finite scaling factor R_{R-M}/R deviating from unity is understood as follows. Even though the Rantz−Marshall formula accounts for the diffusive transport coupled to the flow field, it describes the deposition rate onto a *single* sphere under a uniform flow, thereby not involving the interference effect of the droplet train. Suppose the deviation of $1/R$ from the ideal diffusion theory, $1/R_{ideal}$ of eq (12), is attributed to the following two factors, that is, the flow effect and the interference effect, and only the former could be incorporated by the Rantz−Marshall formula. Therefore, comparison between the calculated deposition rate, R, and the Rantz−Marshall rate, R_{R-M}, allows us to extract the pure interference effect after correcting for the flow effect. The nearly constant scaling factor R_{R-M}/R implies that the above correction works fairly well to define the pure interference effect.

The present calculations suggest an alternative model of the gaseous resistance on the basis of the Rantz−Marshall formula. The gas-phase transport in a certain condition in the flow tube is represented by the Rantz−Marshall formula eqs (14) and (15) with the scaling factor $R_{R-M}/R \approx 2.3-2.4$. While this model is derived rather empirically to reproduce the calculated gas-phase

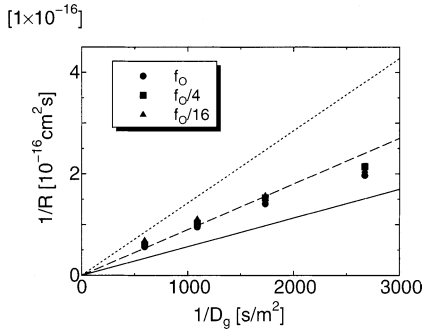

Figure 9. Relation between the inverse diffusion coefficient $1/D_g$ and inverse deposition rate $1/R$ of the model with methanol as the trace gas and varying total pressure P_{total} and orifice frequency f_o at $T = 0$ °C. The circle, square, and triangle points denote f_o, $f_o/4$, and $f_o/16$, respectively. The solid, dashed, and dotted lines refer to the Smoluchowski deposition rate $1/R_{ideal}$ of eq (12) at f_o, $f_o/4$, and $f_o/16$, respectively.

deposition rate, it takes into account both the flow effect and the interference among the droplets explicitly. Note that the scaling factor thus derived, $R_{R-M}/R \approx 2.3-2.4$, is applicable to the droplet geometry depicted in Figure 1 and that the ratio R_{R-M}/R should asymptotically approach unity as the interference loses its influence with an increasing interval between droplets. We also note that this model is valid only in the continuum regime because both the present calculation and the Rantz−Marshall formula eqs (14) and (15) deal with the continuum regime.

3.5. Effects of Orifice Frequency. In the actual experimental conditions, as described in section 2, the liquid surface area in the flow tube is controlled by changing the orifice frequency with a fixed volumetric flow rate and droplet velocity. The total surface area changes with the orifice frequency f_o because both the droplet diameter d and the center-of-mass distance d_c simultaneously vary as $d \propto f_o^{-1/3}$ and $d_c \propto f_o^{-1}$. Usually, the orifice frequency is considered to affect the amount of uptake by changing the total surface area, with an implicit assumption that the deposition rate, normalized by the surface area, is constant. However, changing the droplet diameter and distance could influence the gaseous fields in the flow tube in addition to the total surface area, which might affect the deposition rate. In this subsection, we examine the influence of the orifice frequency on the deposition rate.

Figure 9 shows the calculated deposition rates at the frequencies f_o, $f_o/4$, and $f_o/16$. The orifice frequency, the droplet diameter, and the droplet center-of-mass distance in the three cases are summarized below.

	frequency (kHz)	diameter (μm)	distance (μm)
f_o	100	113	270
$f_o/4$	25	180	1080
$f_o/16$	6.25	285	4320

The first set of conditions corresponds to the Rayleigh natural breakup condition, eq (8). In the three cases, the results plotted in Figure 9 reveal that the deposition rates are surprisingly insensitive to the orifice frequency. This fact has been found experimentally by Worsnop et al.,[15] who demonstrated that the gaseous resistance depends on the orifice diameter but not on the droplet diameter. Our calculation supports this experimental finding and also corroborates the above-mentioned assumption of the experimental analysis[15] that a varying orifice frequency changes the total surface area but not the deposition rate.

Deducing the mechanism that produces invariant deposition rates as a function of the orifice frequency is an interesting

problem. As a clue to the mechanism, we compare the calculated rates to the ideal Smoluchowski rates from eq (12), depicted also in Figure 9 by the three lines. Note that the Smoluchowski diffusive rate of eq (12) varies with the frequency through the variation in droplet diameter, d. While the calculated rates are nearly invariant to the orifice frequency, the ideal diffusive resistances become larger with decreasing frequency. Consequently, Figure 9 indicates that the calculated rates are *faster* than the ideal diffusive rates at lower frequencies. This acceleration is attributed to the flow effect that facilitates the deposition, as discussed in detail in the preceding subsection. As the orifice frequency decreases, the distance between adjacent droplets grows more rapidly ($\propto f_o^{-1}$) compared to the droplet diameter ($\propto f_o^{-1/3}$). Therefore, the interference among droplets, which suppresses the deposition rate, becomes increasingly less significant at lower frequencies.

The invariant deposition rates could be caused by two opposing factors, that is, the droplet diameter, d, and the droplet spacing, d_c. As the orifice frequency decreases, the droplet diameter grows so as to hinder the diffusive transport, represented in the Smoluchowski formula eq (12). On the other hand, the droplet spacing increases with lower frequency so that the decreasing interference effect among the droplets facilitates the gaseous transport. The apparent insensitivity consequently emerges as the two factors change simultaneously with the orifice frequency in fixed and quantitative relationships: $d \propto f_o^{-1/3}$ and $d_c \propto f_o^{-1}$.

4. Concluding Remarks

As an experimental method to study the mass-accommodation kinetics at liquid−vapor interfaces, the droplet-train/flow-reactor technique has several unique virtues as described in section 1. A significant problem, however, lies in the subsequent analysis to decompose the phenomenological uptake rate into elemental kinetic steps, as is common for the other experimental methods of heterogeneous kinetics. We think that theoretical simulation can significantly benefit the experimental analyses, particularly when the decomposition is not straightforward based on experimental information. In this paper, we have focused on the kinetic step of gas-phase transport in the droplet-train/flow-reactor apparatus because the analytical expression of the gas-phase resistance in a droplet-train flow tube has not been established.

It is known that the Fuchs−Sutugin formula well describes the gas-phase resistance for uptake onto a droplet over a wide range of Knudsen numbers. However, because the Fuchs−Sutugin formula has been originally derived from a spherical boundary condition, it is not straightforwardly applied to the actual droplet-train experiments where a train of droplets moves fast in a flow tube. The boundary conditions for the droplet-train flow tube are far more complicated than the ideal condition that a single spherical droplet is present in a quiescent gaseous media and even more complicated than those of other techniques using the Knudsen-cell reactor or the coated-wall flow tube. Therefore, we have employed numerical calculations of the coupled-diffusion equation and the fluid dynamics under boundary conditions that mimic the droplet-train flow tube and thereby directly evaluated the gaseous resistance in the flow tube.

The concentration distribution in the flow tube and the deposition rate onto the droplets were discussed in comparison with the above ideal model. The calculated concentration field of the trace species shows a spherical distribution around each droplet only in close proximity of each droplet, whereas the overall concentration distribution assumes a cylindrically symmetric form with the trace species quite depleted near the flow-tube axis in the wake of each droplet. This feature is attributed to fluid dynamical coupling and interference among the droplets, implying that the assumption of an isolated droplet is not suitable. Consequently, the deposition rate in the flow tube is substantially reduced from the above ideal model in the natural breakup conditions. The deviation is determined by two factors, that is, the flow effect and the interference among the droplets. Although the flow (effect of the moving droplets) facilitates the transport onto the droplets, the interference hinders the diffusive transport. As a consequence, the phenomenological uptake coefficient is well represented with the Fuchs−Sutugin formula, provided that the droplet diameter and the mass-accommodation coefficient included in the formula are replaced with the optimized effective parameters.

The deposition rate with varying droplet velocity and orifice frequency were examined, with conditions corresponding to the actual experiments. The deposition rate shows a modest dependence on the droplet velocity, and the dependence is well represented by the Rantz−Marshall formula with a scaling factor of ~2.3−2.4. The nearly invariant scaling factor allows us to define the pure interference effect on the deposition rate after correcting the flow effect. We also found that the deposition rate is surprisingly insensitive to varying orifice frequency. This is a consequence of an interesting cancellation of effects due to the diffusive resistance and the interference among the droplets.

The refined analysis of the gas-phase transport in the flow tube should have significant implications for the droplet experiments with relatively large mass-accommodation coefficients and low Knudsen numbers, for example, water vapor on liquid water. We hope the present analysis will improve the quantitative accuracy and expand the applicability of the droplet-train experiments.

Acknowledgment. The authors thank Drs. Doug Worsnop, Paul Davidovits, Chuck Kolb, and Dave Hanson for stimulating discussion and several useful comments. This work was supported by Grants-in-Aid (Grants 13127104, 13740329, and 14048216) from the Ministry of Education and Science, Japan, and by the AGS (Alliance for Global Sustainability) Project "Regional Climate and Air Quality".

Appendix A. Effect of Droplet Deceleration

The present calculations have assumed a constant droplet velocity, whereas the experimental measurements show that the droplet velocity slows a little along the length of the droplet train. Accordingly, the momentum transfer associated with the droplet deceleration is not accounted for in this simulation. Shi et al.[12] reported that while the decrease in the speed of droplets generated with a 70-μm orifice is only 5% along the axial length of 21 cm, the decrease is 23% in the droplets generated with a 26-μm orifice. In the latter case, this decrease should be taken into account to evaluate the gas−droplet interaction time along the flow tube. Because the present simulation has adopted a $d_o = 60$ μm orifice, it is not likely that the effect of droplet deceleration is remarkable in the configurations employed in the present calculations. However, when the fluid dynamics calculations are applied to configurations with smaller orifices, the deceleration effect should be taken into account. Therefore, we propose a simple but reasonable way to incorporate this effect in the calculations.

A simple way to treat the change in droplet speed is to convolute the steady-state calculations with varying droplet velocity, assuming a local steady state with a constant velocity

at each region in the flow tube. To make this treatment reasonable, the two conditions that follow are required. First, the droplet speed can be considered to be locally constant in the length scale of several droplet intervals. This condition is, in fact, satisfied even in the case of the smaller orifice mentioned above; the decrease is 23%/21 cm ≈ 1.1%/cm. Second, the local steady-state flow fields are well decoupled among the different spatial regions in the flow tube with varying droplet speed. This means that the perturbation induced by the momentum transfer from the droplets to the gas is relaxed fast enough. This condition is usually also satisfied, as shown in the following discussion. The efficiency of the momentum relaxation within the gas is characterized by the kinematic viscosity ν, which is calculated as $\nu = 1.61 \times 10^{-3}$ m^2/s in the typical situation of Figure 2 ($T = 0$ °C, $P_{total} = 25$ Torr, He buffer). The velocity field in Figure 2a, on the other hand, indicates that the perturbed region strongly coupled to the droplet train ranges radially from the flow-tube axis to $y \approx 5.0 \times 10^{-4}$ m, where $1 - 1/e \approx 0.63$, and $v_d = 27$ m/s of the axial velocity is recovered. Accordingly, the momentum relaxation within the perturbed region takes place in a time scale of $\tau_{mom} = y^2/\nu \approx 1.6 \times 10^{-4}$ s. During this time, the droplets move by $v_d\tau_{mom} \approx 4.2 \times 10^{-3}$ m = 4.2 mm, which is sufficiently shorter than the length of the flow tube.

The above discussion has argued that the change in droplet speed can be treated locally in the axial regions of the flow tube. We have discussed the velocity dependence of the deposition rate in section 3.4 and argued that the velocity dependence is fairly modest. Therefore, in simulating the normal conditions of the droplet-train experiments, the effect of the droplet deceleration is expected to have minor influences on the velocity field or deposition rate.

Appendix B. Uncertainties in the Model Calculations

To draw a quantitative comparison with the experiments, the proper error range of the simulation has to be clarified. Here we summarize and discuss possible uncertainties inherent in the computed deposition rates, which stem from both numerical problems in the calculations and missing factors in the modeling. Possible sources of error include the (1) numerical problems associated with the discrete mesh division, (2) calculated diffusion coefficients of the gas species, (3) deviation from the continuum treatment, (4) variation in the deposition rates with respect to the droplet location, (5) droplet deceleration in the flow tube, and (6) internal liquid motion of the droplets. We discuss these factors in the following discussion.

(1) As discussed in section 2, the discrete mesh division involves two sources of numerical error in calculating the flow−concentration field and in extrapolating the concentration field to the droplet surface. The numerical errors of the two sources are estimated to be ∼0.5 and 4%, respectively, in the calculated deposition rates in section 2. The accuracy was evaluated by comparing the numerical values with those obtained through more accurate and intensive test calculations.

(2) The diffusion coefficients of the gas species virtually provide no significant source of error, though the calculated values of the diffusion coefficients may involve some inaccuracy. The principal purpose of this simulation is to obtain the resistance of the gas-phase transport as a function of ingredient parameters, including pressure, droplet velocity, orifice frequency, etc. The main results of this work in Figures 5−9 present relations between the inverse diffusion coefficient $1/D_g$ and the inverse deposition rate $1/R$ or uptake coefficient $1/\gamma$ because the gas-phase resistance is essentially controlled by the diffusion coefficient D_g. As evidenced in Figure 5, at a fixed velocity and frequency, the calculated $1/R$ values under different temperatures and buffer gases and thereby different diffusion coefficients are well scaled in a certain relation on the $1/D_g$ axis. The critical quantity to be compared with experiment is not each calculated value of the deposition rate but a calculated relation, such as that between D_g and R. We have examined the $1/D_g-1/R$ curve by deliberately using different diffusion coefficients and confirmed that the relation is actually robust, although each value of $1/R$ depends on the $1/D_g$ value employed.

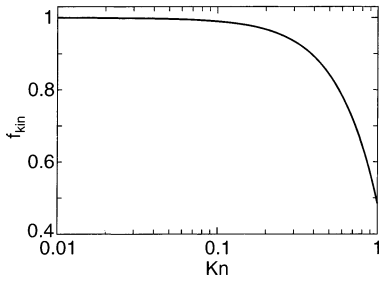

Figure 10. The kinetic correction factor f_{kin}, given by eq (16) as a function of the Knudsen number.

(3) Because the present simulation is based on the continuum treatment of the gas fluid, it is expected that the calculated deposition rate may deviate from the exact value as the Knudsen number becomes larger, where the kinetic molecular collision needs to be explicitly considered. The deviation could be expressed by the kinetic correction factor, f_{kin}, which is given as the ratio of the gaseous resistance based on the continuum treatment to the exact one. In a simple case of the diffusive transport onto a single droplet, where the accurate deposition rate is provided by the Fuchs−Sutugin formula, the kinetic correction factor f_{kin} is given using eqs (6) and (7) as

$$f_{kin} = \frac{0.75/Kn - 0.5}{(0.75 + 0.283Kn)[Kn(1 + Kn)]} \qquad (16)$$

The behavior of f_{kin} is displayed in Figure 10. Note that k_{kin} is almost unity at low Kn, while k_{kin} monotonically decreases with increasing Kn. This indicates that the continuum treatment without the kinetic collision effect tends to underestimate the gaseous resistance (or overestimate the deposition rate) at higher Kn. We can assume that eq (16) well describes the kinetic correction for the uptake in the droplet-train flow tube because the effect of the kinetic collision is essentially local at the droplet surface.

Among the data points in Figure 5, the effect of the kinetic correction may be significant only in the data with small $1/D_g$ values. The condition of the largest Knudsen number ($T = -13$ °C, $P_{total} = 6.0$ Torr, He buffer) has the diffusion coefficient $D_g = 2.88 \times 10^{-3}$ m^2/s, as shown in Table 1. This corresponds to $Kn = 6D_g/\bar{c}d = 0.37$, using $\bar{c} = 414$ m/s and the real droplet diameter $d = 113$ μm. In this extreme case, eq (16) and Figure 10 yield $f_{kin} = 0.91$, indicating that the continuum treatment may underestimate the gaseous resistance by 9%. In the data points at $T = 0$ °C in Figure 6, from which the mass-accommodation coefficient is discussed in section 3.3, all $Kn \leq 0.21$, or $f_{kin} \geq 0.96$, which means that the error due to the kinetic correction is within 4%.

(4) Figure 4 shows that the deposition rate varies with the droplet location, which may cause an uncertainty in the deposition rate. As we discussed in section 3.2, the present values are considered to be an upper limit of the deposition rate. Evaluating the range of error is difficult from the

calculations in this work, but we could estimate it to be within 7−10% from the variation in Figure 4a. (Note that the decrease in the bulk concentration is much smaller within this segment of the flow tube.) This issue will be further discussed in our forthcoming paper.[59]

(5) The effect of the droplet deceleration is discussed in detail in appendix A, where we have argued that this effect can be treated locally in the flow tube. In the conditions of the present simulation, the extent of the droplet deceleration itself is expected to be very small, as discussed in appendix A, and therefore this effect is safely considered to be minor in this work.

(6) The internal liquid circulation induced by the droplet movement can reduce the solubility resistance in the liquid phase and thereby accelerate the overall uptake rate. Although this issue is outside the scope of this paper, it might play a role when comparing the present calculations with experimental results. While this issue has been studied for falling rain droplets in the atmosphere,[2,60] it is not likely that the internal liquid circulation in the low-pressure flow tube is as extensive as that in the atmosphere. As a rough estimation, Baboolal et al.[60] argued that the internal circulation within a single droplet immersed in a gas flow affects the uptake efficiency by 10% in a millisecond order of interaction time at $Re = 4$, a typical Reynolds number for the droplets in the flow tube. However, we can argue that the internal circulation in the droplet train is most likely much less significant than that in a single droplet because the steady movement of the droplet train is much less perturbed by shear friction from the gas, as mentioned in section 3.1.

To summarize the above estimates, we conclude that the calculated deposition rates have an error range $\approx -15\%$ to $+10\%$, with a larger error in the negative direction mainly due to factors 3 and 4. This error range is nearly comparable to the experimental uncertainty.

References and Notes

(1) Seinfeld, J. H.; Pandis, S. N. *Atmospheric Chemistry and Physics*; Wiley: New York, 1998.

(2) Pruppacher, H. R.; Klett, J. D. *Microphysics of Clouds and Precipitation*; Kluwer Academic: Dordrecht, The Netherlands, 1997.

(3) Finlayson-Pitts, B. J.; Pitts, J. N., Jr. *Chemistry of the Upper and Lower Atmosphere*; Academic Press: San Diego, 2000.

(4) *J. Aerosol Sci.* **2001**, *32* (7).

(5) Kolb, C. E.; Worsnop, D. R.; Zahniser, M. S.; Davidovits, P.; Keyser, L. F.; Leu, M. T.; Molina, M. J.; Hanson, D. R.; Ravishankara, A. R. Laboratory Studies of Atmospheric Heterogeneous Chemistry. In *Progress and Problems in Atmospheric Chemistry*; Baker, J. R., Ed.; World Scientific: Singapore, 1995.

(6) Fenter, F. F.; Caloz, F.; Rossi, M. J. *J. Phys. Chem.* **1994**, *98*, 9801−9810.

(7) Beichert, P.; Finlayson-Pitts, B. J. *J. Phys. Chem.* **1996**, *100*, 15218−15228.

(8) Hudson, P. K.; Zondlo, M. A.; Tolbert, M. A. *J. Phys. Chem. A* **2002**, *106*, 2882−2888.

(9) Iraci, L. T.; Essin, A. M.; Golden, D. M. *J. Phys. Chem. A* **2002**, *106*, 4054−4060.

(10) Worsnop, D. R.; Zahniser, M. S.; Kolb, C. E.; Gardner, J. A.; Watson, L. R.; Van Doren, J. M.; Jayne, J. T.; Davidovits, P. *J. Phys. Chem.* **1989**, *93*, 1159−1172.

(11) Jayne, J. T.; Duan, S. X.; Davidovits, P.; Worsnop, D. R.; Zahniser, M. S.; Kolb, C. E. *J. Phys. Chem.* **1991**, *95*, 6329−6336.

(12) Shi, Q.; Li, Y. Q.; Davidovits, P.; Jayne, J. T.; Worsnop, D. R.; Mozurkewich, M.; Kolb, C. E. *J. Phys. Chem. B* **1999**, *103*, 2417−2430.

(13) Swartz, E.; Shi, Q.; Davidovits, P.; Jayne, J. T.; Worsnop, D. R.; Kolb, C. E. *J. Phys. Chem. A* **1999**, *103*, 8824−8833.

(14) Li, Y. Q.; Davidovits, P.; Shi, Q.; Jayne, J. T.; Kolb, C. E.; Worsnop, D. R. *J. Phys. Chem. A* **2001**, *105*, 10627−10634.

(15) Worsnop, D. R.; Shi, Q.; Jayne, J. T.; Kolb, C. E.; Swartz, E.; Davidovits, P. *J. Aerosol Sci.* **2001**, *32*, 877−891.

(16) Katrib, Y.; Deiber, G.; Schweitzer, F.; Mirabel, P.; George, C. *J. Aerosol Sci.* **2001**, *32*, 893−911.

(17) Katrib, Y.; Mirabel, P.; Calvé, S. L.; Weck, G.; Kochanski, E. *J. Phys. Chem. B* **2002**, *106*, 7237−7245.

(18) Hanson, D. R.; Ravishankara, A. R. *J. Phys. Chem.* **1993**, *97*, 12309−12319.

(19) Zhang, R.; Jayne, J. T.; Molina, M. J. *J. Phys. Chem.* **1994**, *98*, 867−874.

(20) Davies, J. A.; Cox, R. A. *J. Phys. Chem. A* **1998**, *102*, 7631−7642.

(21) Waschewski, G. C. G.; Abbatt, J. P. D. *J. Phys. Chem. A* **1999**, *103*, 5312−5320.

(22) Huff, A. K.; Abbatt, J. P. D. *J. Phys. Chem. A* **2002**, *106*, 5279−5287.

(23) Müller, B.; Heal, M. R. *J. Phys. Chem. A* **2002**, *106*, 5120−5127.

(24) Mozurkewich, M.; McMurry, P. H.; Gupta, A.; Calvert, J. G. *J. Geophys. Res.* **1987**, *92*, 4163.

(25) Mozurkewich, M.; Calvert, J. G. *J. Geophys. Res.* **1988**, *93*, 15889.

(26) Lovejoy, E. R.; Hanson, D. R. *J. Phys. Chem.* **1994**, *99*, 2080.

(27) Hanson, D. R.; Lovejoy, E. R. *J. Phys. Chem.* **1996**, *100*, 6397−6405.

(28) Kirchner, W.; Welter, F.; Bongartz, A.; Kaines, J.; Schweighoefer, S.; Schurath, U. *J. Atmos. Chem.* **1990**, *10*, 427−449.

(29) Shimono, A.; Koda, S. *J. Phys. Chem.* **1996**, *100*, 10269−10276.

(30) Schwartz, S. E. In *Chemistry of Multiphase Atmospheric Systems*; Jaescke, W., Ed.; Springer-Verlag: Berlin, 1986; Vol. G6.

(31) Wilson, M. A.; Pohorille, A. *J. Phys. Chem. B* **1997**, *101*, 3130−3135.

(32) Taylor, R. S.; Garrett, B. C. *J. Phys. Chem. B* **1999**, *103*, 844−851.

(33) Hanson, D. R.; Kosciuch, E. *J. Phys. Chem.* **2002**, submitted for publication.

(34) Davidovits, P.; Jayne, J. T.; Duan, S. X.; Worsnop, D. R.; Zahniser, M. S.; Kolb, C. E. *J. Phys. Chem.* **1991**, *95*, 6337−6340.

(35) Davidovits, P.; Hu, J. H.; Worsnop, D. R.; Zahniser, M. S.; Kolb, C. E. *Faraday Discuss.* **1995**, *100*, 65−82.

(36) Mozurkewich, M. *Aerosol Sci. Technol.* **1986**, *5*, 223−236.

(37) Marek, R.; Straub, J. *Int. J. Heat Mass Transfer* **2001**, *44*, 39−53.

(38) Wagner, P. E. Aerosol Growth by Condensation. In *Aerosol Microphysics II, Chemical Physics of Microparticles*; Marlow, W. H., Ed.; Springer-Verlag: Berlin, 1982.

(39) Majerowicz, A.; Wagner, P. E. Experiments on the sticking probability for water molecules during condensation of water vapor in air. In *Atmospheric Aerosols and Nucleation*; Wagner, P. E., Vali, G., Eds.; Springer-Verlag: Berlin, 1988; Vol. 309.

(40) Hanson, D. R. *J. Phys. Chem. B* **1997**, *101*, 4998−5001.

(41) Vesala, T.; Hannemann, A. U.; Luo, B. P.; Kulmala, M.; Peter, Th. *J. Aerosol Sci.* **2001**, *32*, 843−860.

(42) Danckwerts, P. V. *Gas−Liquid Reactions*; McGraw-Hill: New York, 1970.

(43) Fuchs, N. A.; Sutugin, A. G. *Highly Dispersed Aerosols*; Ann Arbor Science Publishers: Ann Arbor, MI, 1970.

(44) Hanson, D. R.; Ravishankara, A. R.; Lovejoy, E. R. *J. Geophys. Res.* **1996**, *101*, 9063−9069.

(45) Motz, H.; Wise, H. *J. Chem. Phys.* **1960**, *32*, 1893−1894.

(46) Widmann, J. F.; Davis, E. J. *J. Aerosol Sci.* **1997**, *28*, 1233−1249.

(47) Sugiyama, M.; Koda, S.; Morita, A. *Chem. Phys. Lett.* **2002**, *362*, 56−62.

(48) Lide, D. R., Ed. *Handbook of Chemistry and Physics*, 81st ed.; CRC Press: Boca Raton, FL, 2000.

(49) Smoluchowski, M. *Z. Phys. Chem.* **1918**, *92*, 129−168.

(50) Collins, F. C.; Kimball, G. E. *J. Colloid Sci.* **1949**, *4*, 425−437.

(51) Ibuki, K.; Ueno, M. *Bull. Chem. Soc. Jpn.* **1997**, *70*, 543−553.

(52) Hirschfelder, J. O.; Curtiss, C. F.; Bird, R. B. *Molecular Theory of Gases and Liquids*; Wiley: New York, 1954.

(53) McQuarrie, D. A. *Statistical Mechanics*; University Science Books: Sausalito, CA, 2000.

(54) Reid, R. C.; Sherwood, T. K. *The Properties of Gases and Liquids*, 2nd ed.; McGraw-Hill: New York, 1966.

(55) *FLUENT 5.5*; Fluent, Inc.: Lebanon, NH, 2000.

(56) Rantz, W. E.; Marshall, W. R. *Chem. Eng. Prog.* **1952**, *48*, 141−146.

(57) Kulmala, M.; Wagner, P. E. *J. Aerosol Sci.* **2001**, *32*, 833−841.

(58) We have examined the other boundary condition, $k^{int} = \bar{c}/2$, and confirmed that the finite rate of k^{int} augments the uptake resistance ($1/\gamma$) by 1/2 almost uniformly, which is consistent to the resistance model, eq (3).

(59) Morita, A.; Sugiyama, M.; Kameda, H.; Koda, K., paper in preparation.

(60) Baboolal, L. B.; Pruppacher, H. R.; Topalian, J. H. *J. Atmos. Sci.* **1981**, *38*, 856−870.